UC Berkeley

UC Berkeley Previously Published Works

Title

Effect of Solvent Motion on Ion Transport in Electrolytes

Permalink

https://escholarship.org/uc/item/11w6v7vv

Journal

Journal of The Electrochemical Society, 169(4)

ISSN

0013-4651

Authors

Mistry, Aashutosh
Grundy, Lorena S
Halat, David M
et al.

Publication Date

2022-04-01

DOI

10.1149/1945-7111/ac6329

Copyright Information

This work is made available under the terms of a Creative Commons Attribution-NonCommercial License, available at https://creativecommons.org/licenses/by-nc/4.0/

Peer reviewed

eScholarship.org Powered by the California Digital Library
University of California

Effect of Solvent Motion on Ion Transport in Electrolytes

Aashutosh MISTRY,[1,2,a,z] Lorena S. GRUNDY,[3,4,b] David M. HALAT,[3,4,5,c] John NEWMAN,[3,y] Nitash P. BALSARA[3,4,5,d,z,*] and Venkat SRINIVASAN[1,2,6,e,z,*]

[1] Chemical Sciences and Engineering Division, Argonne National Laboratory, Lemont, Illinois 60439, United States
[2] Joint Center for Energy Storage Research, Argonne National Laboratory, Lemont, Illinois 60439, United States
[3] Department of Chemical and Biomolecular Engineering, University of California, , Berkeley, California 94720, United States
[4] Joint Center for Energy Storage Research, Lawrence Berkeley National Laboratory, Berkeley, California 94720, United States
[5] Materials Sciences Division, Lawrence Berkeley National Laboratory, Berkeley, California 94720, United States
[6] Argonne Collaborative Center for Energy Storage Science, Argonne National Laboratory, Lemont, Illinois 60439, United States

Abstract We use concentrated solution theory to derive an equation governing solvent velocity in a binary electrolyte when a current passes through it. This equation in combination with the material balance equation enables the prediction of electrolyte concentration profiles and ion velocities as a function of space and time. This framework is used to predict ion velocities in Li-Li symmetric cells containing a mixture of lithium bis(trifluoromethanesulfonyl)imide and poly(ethylene oxide) (LiTFSI/PEO), for which the cation transference number relative to the solvent velocity, t_+^0, can be either positive or negative in LiTFSI/PEO mixtures, depending on salt concentration. Accounting for the solvent motion is increasingly important at higher concentrations. Especially for negative t_+^0, if solvent velocity is set to zero, the cation velocity, based on the electrode-electrolyte interface reference frame, is pointed opposite to the current flow. However, when solvent motion is taken into account, the cation velocity, based on the same reference frame, is in the same direction as the current. This analysis demonstrates the importance of accounting for solvent velocity rigorously in seemingly simple systems such as symmetric cells.

Understanding ion transport in electrolytes is essential[1] for the rational design of next-generation battery chemistries such as metal anodes[2–6], sulfur cathodes[7,8], and redox-flow batteries[9]. Ion transport is also critical to emerging applications of Li-ion batteries[10–12], for example, extreme fast charging[13–16] and cold-start[17]. Ion transport in binary electrolytes comprising dissociated cations and anions in a solvent is governed by three transport coefficients: ionic conductivity, κ, salt diffusivity, D, and cation transference number with

[*] Corresponding authors: nbalsara@berkeley.edu (NPB) and vsrinivasan@anl.gov (VS)
[a] ORCID: 0000 – 0002 – 4359 – 4975
[b] ORCID: 0000 – 0001 – 7706 – 2216
[c] ORCID: 0000 – 0002 – 0919 – 1689
[d] ORCID: 0000 – 0002 – 0106 – 5565
[e] ORCID: 0000 – 0002 – 1248 – 5952
[y] Electrochemical Society Fellow and Honorary Member
[z] Electrochemical Society Member

respect to the solvent, t_+^0. Figure 1 shows a simple schematic of a Li-Li symmetric cell containing a binary electrolyte. We begin by developing coupled equations that account for ion and solvent motion. Our objective is to quantify the time dependence of ion velocities obtained when a constant current density, i, flows through the cell. We show that these velocities are dependent on solvent motion. In addition to the three transport coefficients, we need knowledge of two additional concentration-dependent thermodynamic properties: electrolyte density and thermodynamic factor. An electrolytic system where all of the necessary properties have been measured[18–20] over a wide range of concentrations is poly(ethylene oxide) (PEO) mixed with lithium bis(trifluoromethanesulfonyl)imide (LiTFSI). An interesting feature of this electrolyte is that t_+^0 is positive at some concentrations and negative at other concentrations. We solve the governing equations under both circumstances, and find surprisingly different results.

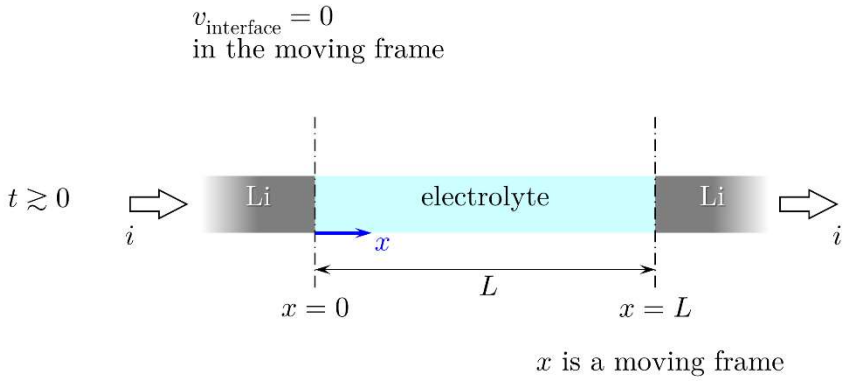

Figure 1. A schematic diagram of a polarized Li-Li symmetric cell. Our analysis is based on a moving frame attached to the electrode-electrolyte interface at $x = 0$.

Theory

The passage of current through the symmetric cell in Figure 1 will result in the motion of the ions and solvent molecules in the electrolytic solution and the electrode-electrolyte interfaces will be displaced. Let v' refer to the velocities measured from a stationary reference frame. The passage of current through the cell in the $+x$ direction will result in the translation of the stripping electrode-electrolyte interface in the $-x$ direction. The velocity of this interface is given by (symbols are explained in Nomenclature):

$$v'_{\text{interface}} = -\frac{M_{\text{Li}} i}{z_+ F \rho_{\text{Li}}}. \qquad [1]$$

In the discussion that follows, all velocities, v_+, v_- and v_0, are measured with respect to this moving reference frame.

Concentrated solution theory[21] gives an expression for the salt material balance (Eq. 12.14 in [1]):

$$\frac{\partial c}{\partial t} = \frac{\partial}{\partial x}\left(D\left(1 - \frac{\mathrm{d}\ln c_0}{\mathrm{d}\ln c}\right)\frac{\partial c}{\partial x}\right) - \frac{i}{\nu_+ z_+ F}\frac{\partial t_+^0}{\partial x} - \frac{\partial (c v_0)}{\partial x}\,. \qquad [2]$$

A similar expression can be written for the solvent material balance:

$$\frac{\partial c_0}{\partial t} = -\frac{\partial (c_0 v_0)}{\partial x}\,. \qquad [3]$$

The definitions of partial molar volumes[1] give

$$c\bar{V} + c_0\bar{V}_0 = 1\,. \qquad [4]$$

With the Gibbs-Duhem expression for partial molar volumes[1,22], *i.e.*, $c\nabla\bar{V} + c_0\nabla\bar{V}_0 = 0$, Eq. [4] can be rearranged as

$$\bar{V}\frac{\partial c}{\partial t} + \bar{V}_0\frac{\partial c_0}{\partial t} = 0\,. \qquad [5]$$

Substitution of Eqs. [2] and [3] into Eq. [5] gives:

$$\frac{\partial v_0}{\partial x} = \bar{V}\left(\frac{\partial}{\partial x}\left(D\left(1 - \frac{\mathrm{d}\ln c_0}{\mathrm{d}\ln c}\right)\frac{\partial c}{\partial x}\right) - \frac{i}{\nu_+ z_+ F}\frac{\partial t_+^0}{\partial x}\right). \qquad [6]$$

Eq. [6] is an important new result. Eqs. [2] and [6] form a complete set that must be solved simultaneously to compute salt concentration and solvent velocity profiles.

The corresponding expression for the ionic current is

$$i = -\kappa\left(\frac{\partial \phi}{\partial x} - \frac{\nu}{\nu_+ z_+}\frac{RT}{F}(1 - t_+^0)\left(1 + \frac{\mathrm{d}\ln f_\pm}{\mathrm{d}\ln c}\right)\frac{\partial \ln c}{\partial x}\right). \qquad [7]$$

Boundary Conditions

At the stripping (left) boundary in Figure 1,

$$v_0 = 0 \text{ at } x = 0\,, \qquad [8]$$

because the electrodes are impermeable to the solvent and the cation flux, N_+, is given by (based on Eq. 12.8 in [1])

$$N_+ = -\nu_+ D\left(1 - \frac{\mathrm{d}\ln c_0}{\mathrm{d}\ln c}\right)\frac{\partial c}{\partial x} + t_+^0\frac{i}{z_+ F} + \nu_+ c v_0\,. \qquad [9]$$

Combining Eqs. [8] and [9], we get

$$N_+ = \frac{i}{z_+ F} = -\nu_+ D\left(1 - \frac{\mathrm{d}\ln c_0}{\mathrm{d}\ln c}\right)\frac{\partial c}{\partial x} + t_+^0\frac{i}{z_+ F} \text{ at } x = 0\,. \qquad [10]$$

Rearrangement gives,

$$-D\left(1-\frac{\mathrm{d}\ln c_0}{\mathrm{d}\ln c}\right)\frac{\partial c}{\partial x}=(1-t_+^0)\frac{i}{\nu_+ z_+ F}\ \text{at}\ x=0\,. \qquad [11]$$

The plating (right) boundary, when viewed from a reference frame attached to the stripping electrode, can move due to expansion or contraction of the electrolyte, *i.e.*, changes in L. The boundary conditions at the plating electrode are

$$c_0 v_0 = c_0\frac{dL}{dt}\ \text{at}\ x=L\,, \qquad [12]$$

$$-\nu_+ D\left(1-\frac{\mathrm{d}\ln c_0}{\mathrm{d}\ln c}\right)\frac{\partial c}{\partial x}+t_+^0\frac{i}{z_+F}+\nu_+ c v_0=\frac{i}{z_+F}+\nu_+ c\frac{dL}{dt}\ \text{at}\ x=L\,. \qquad [13]$$

The electrolyte thickness does not change if its density varies linearly with salt concentration. The dependence of the density of LiTFSI/PEO mixtures as a function of c is presented in Figure 2(a). We show in Appendix A that the change in electrolyte thickness in LiTFSI/PEO is less than 0.1%. We, therefore, neglect the relative motion of the plating electrode. This is an important assumption since it avoids coordinate transformation associated with moving boundary problems[23–25]. Thus, the plating boundary conditions simplify to

$$v_0 = 0\ \text{at}\ x=L\,, \qquad [14]$$

$$-D\left(1-\frac{\mathrm{d}\ln c_0}{\mathrm{d}\ln c}\right)\frac{\partial c}{\partial x}=(1-t_+^0)\frac{i}{\nu_+ z_+ F}\ \text{at}\ x=L\,. \qquad [15]$$

Initial Conditions

We start from an equilibrium state of uniform salt concentration,

$$c(x,t=0)=c_{\text{avg}}\,. \qquad [16]$$

In Figure 2(b), we show the dependence of c_0 on c for LiTFSI/PEO. Thus, specifying the initial concentration, $c(x,t=0)$ also specifies $c_0(x,t=0)=c_{0,\text{avg}}$.

Consider a finite volume of thickness Δx such that its left interface is attached to the Li surface at $x=0$ in Figure 1. Integration of Eq. [6] over this volume gives

$$\begin{aligned} v_0(x=\Delta x,t)-v_0(x=0,t) \qquad [17]\\ =\bar{V}\left\{\left(-D\left(1-\frac{\mathrm{d}\ln c_0}{\mathrm{d}\ln c}\right)\frac{\partial c}{\partial x}+t_+^0\frac{i}{\nu_+ z_+ F}\right)\Big|_{x=0}\right.\\ \left.-\left(-D\left(1-\frac{\mathrm{d}\ln c_0}{\mathrm{d}\ln c}\right)\frac{\partial c}{\partial x}+t_+^0\frac{i}{\nu_+ z_+ F}\right)\Big|_{x=\Delta x}\right\}. \end{aligned}$$

Substitute for boundary conditions from Eqs. [8] and [11],

$$v_0(x=\Delta x,t)=\bar{V}\left\{\left((1-t_+^0)\frac{i}{\nu_+ z_+ F}+t_+^0\frac{i}{\nu_+ z_+ F}\right)\right|_{x=0} - \left(-D\left(1-\frac{\mathrm{d}\ln c_0}{\mathrm{d}\ln c}\right)\frac{\partial c}{\partial x}+t_+^0\frac{i}{\nu_+ z_+ F}\right)\Big|_{x=\Delta x}\Bigg\}. \quad [18]$$

At a short time after the current is turned on, the concentration is still uniform in the electrolyte, and the concentration gradient at $x=\Delta x$ can be ignored. Eq. [18] thus simplifies to,

$$v_0(x=\Delta x,t=0)=\bar{V}(1-t_+^0)\frac{i}{\nu_+ z_+ F}. \quad [19]$$

Eq. [19] is valid for any value of Δx within the electrolyte. Thus,

$$v_0(0<x<L,t=0)=\bar{V}(1-t_+^0)\frac{i}{\nu_+ z_+ F}. \quad [20]$$

We note that, in our model, the solvent motion begins, *i.e.*, $v_0\neq 0$, as soon as the current is applied; acceleration of the solvent molecules from the rest state is assumed to occur on extremely rapid time scales.

To summarize, the governing equations for determining the dependence of c and v_0 on x,t are Eqs. [2] and [6]. The boundary conditions for c are Eqs. [11] and [15], and those for v_0 are Eqs. [8] and [14]. The initial conditions of these variables are prescribed by Eqs. [16] and [20]. Note that while v_0 governing equation only requires one v_0 boundary condition and no initial condition, to solve the governing equation for salt concentration, c, both v_0 boundary conditions as well as v_0 initial condition are required.

Solving for $c(x,t)$ and $v_0(x,t)$ permits calculation of the local ion velocities, v_+ and v_-, using the equations

$$v_+=-\frac{1}{c}D\left(1-\frac{\mathrm{d}\ln c_0}{\mathrm{d}\ln c}\right)\frac{\partial c}{\partial x}+\frac{1}{c}t_+^0\frac{i}{\nu_+ z_+ F}+v_0, \quad [21]$$

$$v_-=-\frac{1}{c}D\left(1-\frac{\mathrm{d}\ln c_0}{\mathrm{d}\ln c}\right)\frac{\partial c}{\partial x}-\frac{1}{c}(1-t_+^0)\frac{i}{\nu_+ z_+ F}+v_0. \quad [22]$$

Eqs. [21], [22] are obtained by rearranging the general expressions for ion fluxes, e.g., Eq. [9].

Using $c(x,t)$ in Eq. [7], the electric potential difference across the electrolyte is obtained as

$$\Delta\phi=\phi_0-\phi_L=i\int_L^0\frac{1}{\kappa}\mathrm{d}x+\frac{\nu}{\nu_+ z_+}\frac{RT}{F}\int_L^0(1-t_+^0)\left(1+\frac{\mathrm{d}\ln f_\pm}{\mathrm{d}\ln c}\right)\mathrm{d}\ln c. \quad [23]$$

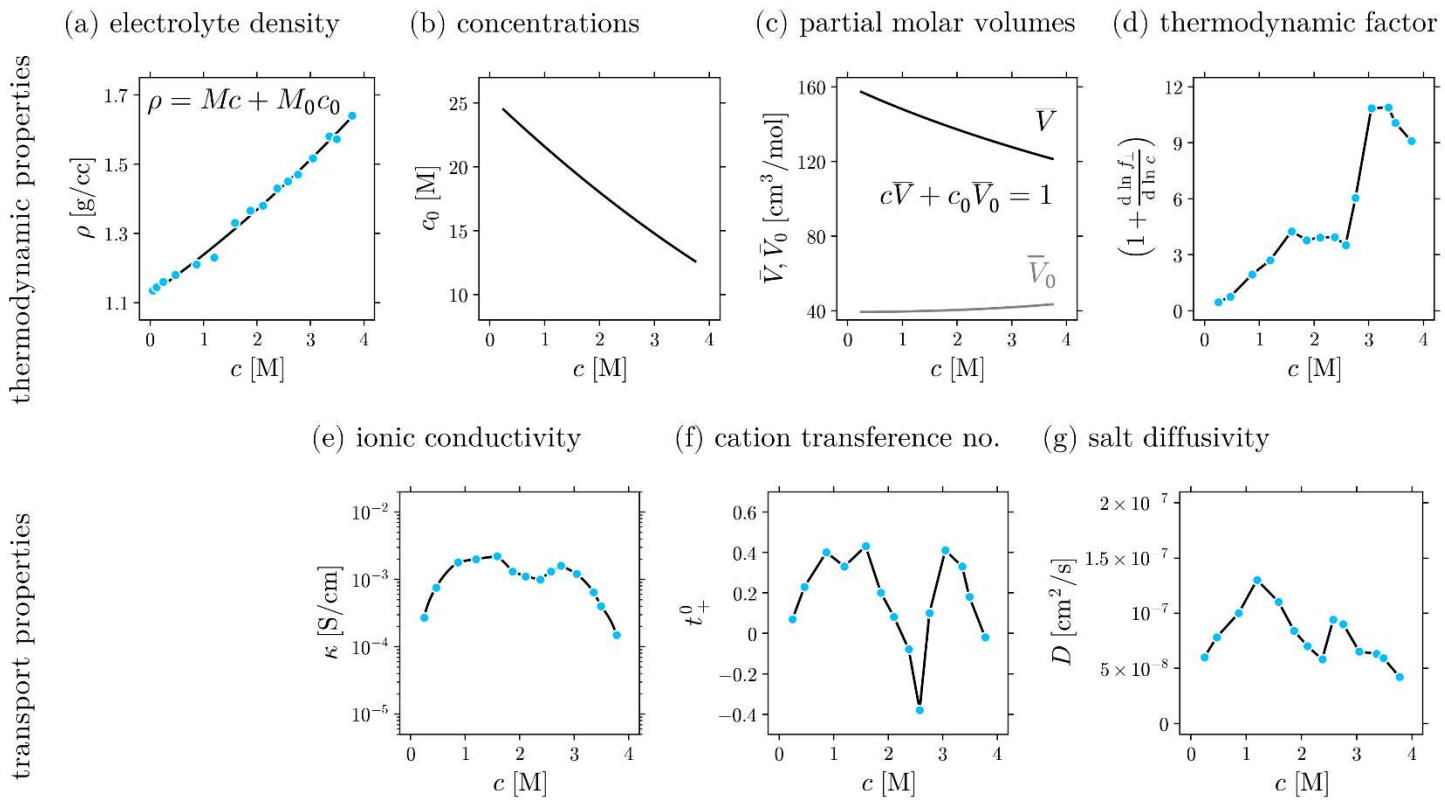

Figure 2. Thermodynamic and transport properties of the LiTFSI/PEO electrolyte at 90°C used for calculations. (a) The electrolyte density measurements (symbols) are fitted to an analytical expression (Eq. [26]) to obtain (c) partial molar volumes. (b) The density versus salt concentration curve can be alternatively expressed as solvent concentration versus salt concentration curve. Concentration dependence of (d) thermodynamic factor, (e) ionic conductivity, (f) cation transference number with respect to the solvent velocity, and (g) salt diffusivity are shown.

Our framework applies to any binary electrolyte, provided all the properties in the governing equations are known functions of concentration. This is the case for LiTFSI/PEO mixtures. The dependence of $\bar{V}$, thermodynamic factor, κ, t_+^0, and D are given in Figure 2(c)-(g). The measured values of these properties, necessary for our calculations, are also listed in **Error! Not a valid bookmark self-reference.**.

Table 1 . Thermodynamic and transport properties of LiTFSI/PEO at 90°C taken from the literature; Table I in reference [19], Table II in reference [20], and Table A1 in reference [18].

c (M)	ρ (g/cm^3)	t_+^0	κ (S/cm)	D (cm^2/s)	$\left(1+\frac{\mathrm{d}\ln f_{\pm}}{\mathrm{d}\ln c}\right)$
0.25	1.160	0.07	2.7×10^{-4}	6.0×10^{-8}	0.45
0.47	1.180	0.23	7.5×10^{-4}	7.8×10^{-8}	0.75
0.87	1.210	0.40	1.8×10^{-3}	1.0×10^{-7}	1.93
1.20	1.230	0.33	2.0×10^{-3}	1.3×10^{-7}	2.69
1.59	1.330	0.43	2.2×10^{-3}	1.1×10^{-7}	4.24
1.87	1.365	0.20	1.3×10^{-3}	8.4×10^{-8}	3.78
2.11	1.380	0.08	1.1×10^{-3}	7.0×10^{-8}	3.92
2.38	1.430	−0.08	9.9×10^{-4}	5.8×10^{-8}	3.93
2.58	1.450	−0.38	1.3×10^{-3}	9.4×10^{-8}	3.51
2.76	1.470	0.10	1.6×10^{-3}	9.0×10^{-8}	6.03
3.05	1.516	0.41	1.2×10^{-3}	6.5×10^{-8}	10.84
3.36	1.580	0.33	6.4×10^{-4}	6.3×10^{-8}	10.89
3.49	1.572	0.18	4.0×10^{-4}	5.9×10^{-8}	10.06
3.78	1.640	−0.02	1.5×10^{-4}	4.2×10^{-8}	9.08

Our approach, which uses the solvent velocity as a reference, is not unique. An alternative form of the concentrated solution theory uses the volume average velocity, $v^{\blacksquare}$, as the reference[26–30]. This approach requires knowledge of the partial molar volumes of the ions, $\bar{V}_+, \bar{V}_-$, which cannot be measured experimentally. Instead our approach requires the partial molar volume of salt, which is straightforward to measure experimentally.

In general, solvent motion can be induced by several mechanisms. Mechanisms involving a net force acting on the electrolyte volume cause fluid flow, and the corresponding velocities are influenced by viscosity, for example, rotating ring electrode[31], pressure-driven flow[32–34], natural convenction[35], electro-convection[1,36], *etc*. Such instances would require us

to solve for the Navier-Stokes Equation in clear media or alternatively Darcy's law in porous media to account for fluid flow in response to external forces. However, the system studied here is assumed to be at a constant temperature and pressure, and the solvent motion is thus not induced by such effects. The uniform temperature field also suppresses the thermophoretic motion[1]. Under such conditions, it can be shown that the traditional governing equations for fluid motion are trivially satisfied. The mode of solvent transport discussed here arises entirely due to the diffusion and migration of ionic species driven by the electric field. As a result, such motion is not influenced by viscosity and is observed even in the highly viscous LiTFSI/PEO mixtures discussed here. This mode of solvent motion is equivalent to electroosmotic drag in the fuel cell literature[37,38]. In general, this mode contributes to the flux of charge neutral species when the electric field causes ion motion, for example, transport of dissolved oxygen in a Li-oxygen electrolyte[39]. The fundamental driving force for such motion is the frictional coupling between ions and neutral species that is captured by the Stefan-Maxwell formalism of diffusion and is the central argument of Newman's concentrated solution theory[8,37–40].

Results and Discussion

The governing equations with appropriate boundary and initial conditions were solved using the Finite Volume Method (Appendix B). Appropriate numerical parameters, $\Delta x = 10\ \mu$m and $\Delta t = 0.1$ s, are chosen such that their effect on the solution is negligible. The electrolyte thickness is 500 μm. The properties measured at discrete values of c were converted into continuous variables by linear interpolation (see Figure 2). The quadratic fit through the ρ versus c (Figure 2(a) and Eq. [26]) data specifies the dependence of $c_0, \bar{V}, \bar{V}_0$, and $\left(1 - \frac{\mathrm{d}\ln c_0}{\mathrm{d}\ln c}\right)$ on c (Eqs. [29] through [32] in Appendix C).

Figure 3 shows the spatial and temporal variations of c and c_0 starting with two electrolytes with uniform concentrations, $c_{\mathrm{avg}} = 1.00$ M and $c_{\mathrm{avg}} = 2.58$ M, polarized at $i = 0.3$ mA/cm^2. These concentrations are chosen as they represent two transference number extremes, $t_+^0 \approx +0.4$ and $t_+^0 \approx -0.4$ as shown in Figure 2(f). Concentrations are shown using a continuous color scale, and constant concentration contour lines are identified to assist visualization. Comparing $c(x,t)$ in Figure 3(a) and (c), the difference in colors used in these two plots is not surprising because of the difference in c_{avg}. However, the contour lines in Figure 3(c) are much more tightly spaced, indicating steeper concentration gradients in the $c_{\mathrm{avg}} = 2.58$ M electrolyte. The contour lines are asymmetrical about $x/L = 0.5$; gradients in the $x/L > 0.5$ region are steeper than in the $x/L < 0.5$ region. The spatial and temporal dependence of c_0 shown in Figure 3(b) and (d) are complementary to the spatial and temporal dependence of c. As seen in Figure 3(a),(c), salt accumulates close to the stripping electrode ($x/L = 0$) and depletes near the plating electrode ($x/L = 1$). Correspondingly, as Figure 3(b),(d) show, solvent depletes near the stripping electrode ($x/L = 0$), and accumulates close to the plating electrode ($x/L = 1$). At a given time, t, every x location in

Figure 3(a) and (c) (or equivalently, in Figure 3(b) and (d)) represents an equilibrium state on the c_0 versus c curve in Figure 2(b).

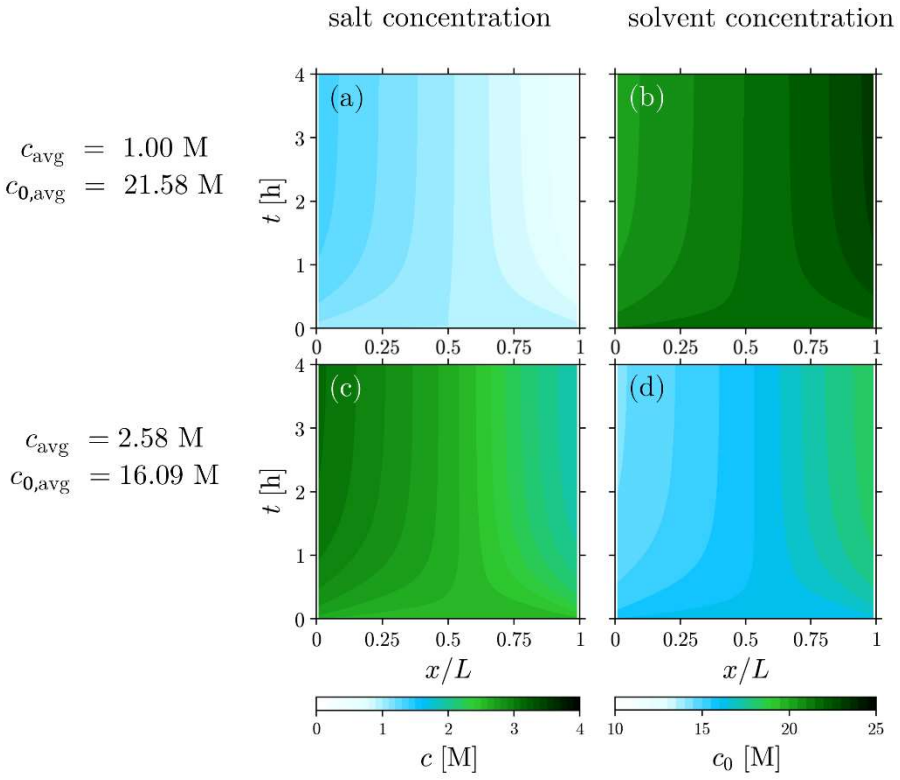

Figure 3. Evolution of (a),(c) salt and (b),(d) solvent concentrations in space and time for an electrolyte polarized at i = 0.3 mA/cm^2. Initial uniform salt concentrations are (a),(b) c_{avg} = 1.00 M ($t_+^0 \approx +0.4$) and (c),(d) c_{avg} = 2.58 M ($t_+^0 \approx -0.4$).

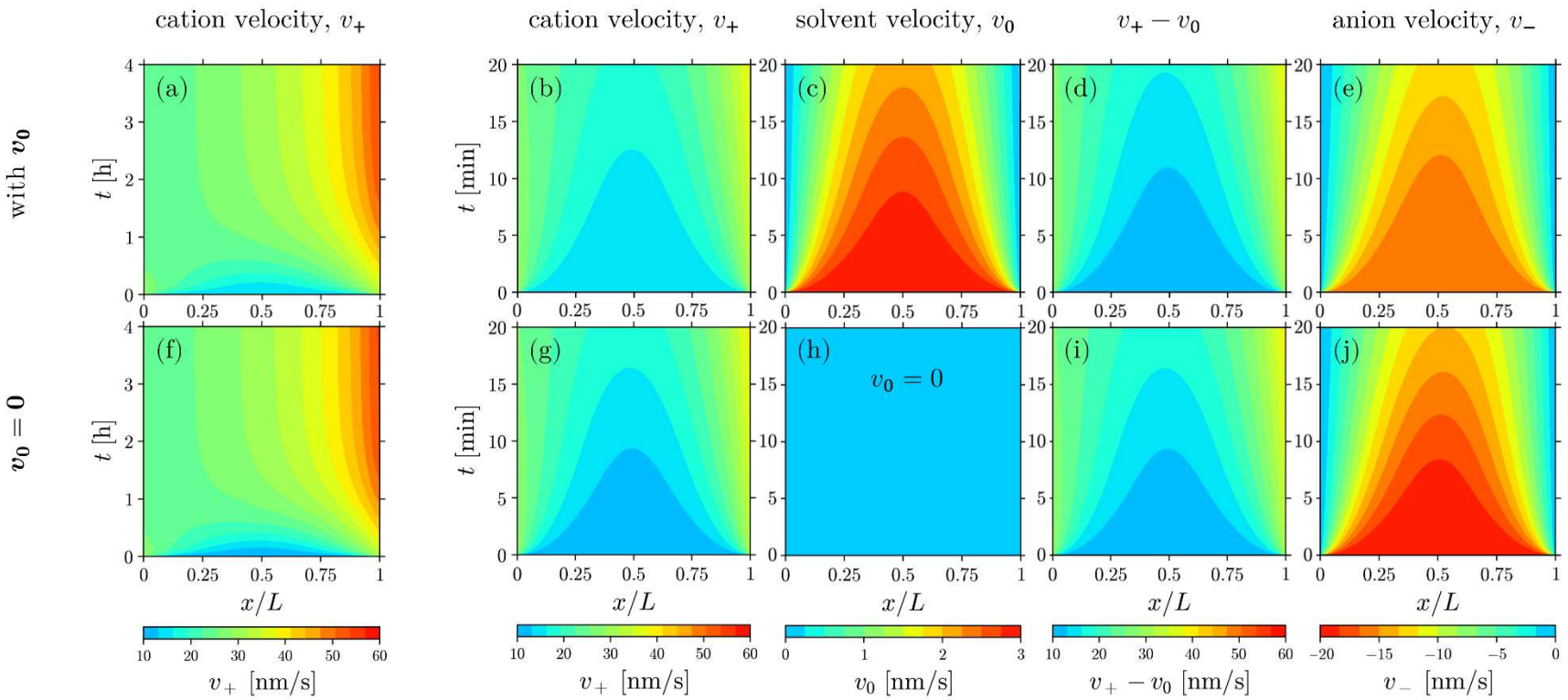

Figure 4. Comparing spatial distribution and time evolution of velocity fields for $c_{\text{avg}} = 1.00$ M LiTFSI/PEO (corresponding to $t_+^0 \approx +0.4$) polarized at $i = 0.3$ mA/cm^2. (a)-(e) with solvent motion and (f)-(j) for $v_0 = 0$. Velocities are with respect to a moving reference frame attached to the electrode-electrolyte interface ($v'_{\text{interface}} = -0.4$ nm/s). The time axis spans 0 to 4 h in (a), (f), and 0 to 20 min for the rest of the plots. Identical velocity color scales are used for the same velocity fields and are shown below the corresponding $v_0 = 0$ plots.

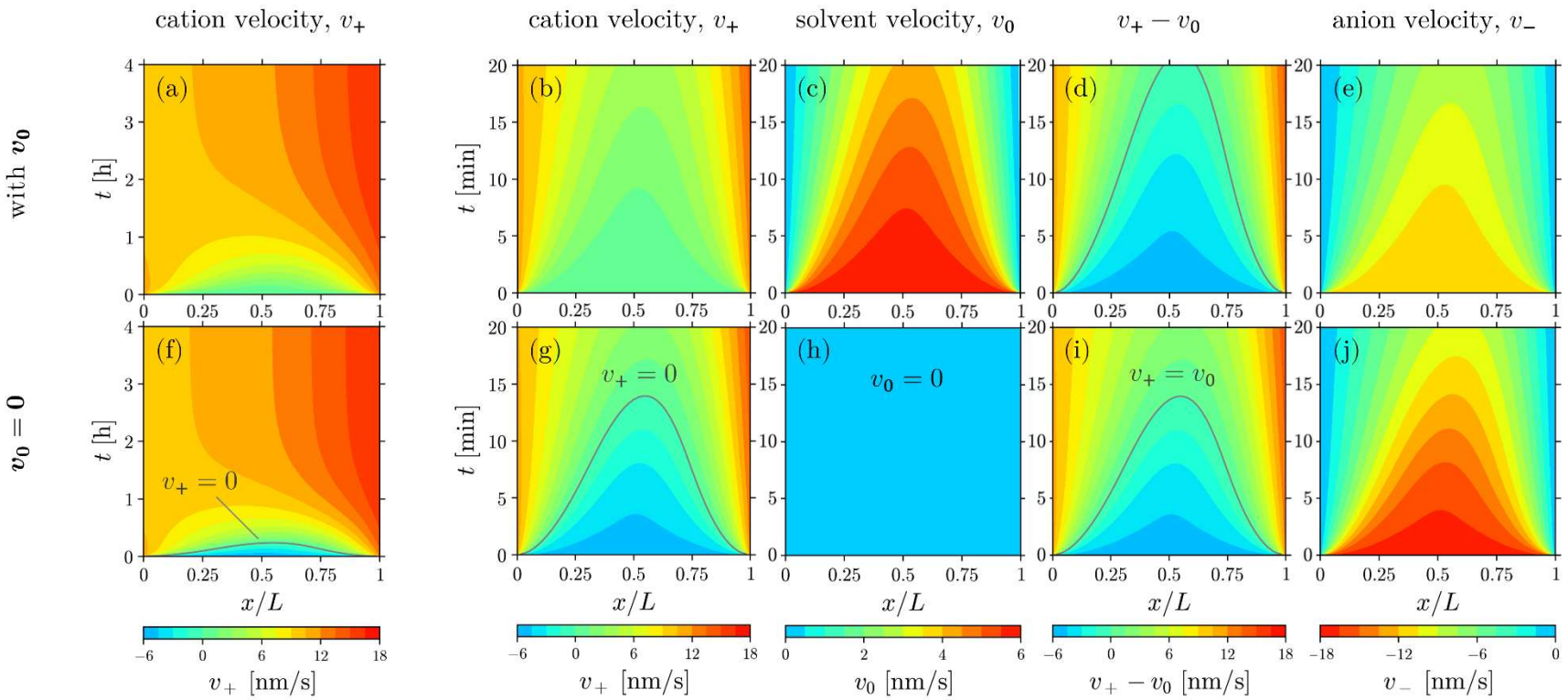

Figure 5. Comparing spatial distribution and time evolution of velocity fields for $c_{\text{avg}} = 2.58$ M LiTFSI/PEO (corresponding to $t_+^0 \approx -0.4$) polarized at $i = 0.3$ mA/cm^2. (a)-(e) with solvent motion and (f)-(j) for $v_0 = 0$. Velocities are with respect to a moving reference frame attached to the electrode-electrolyte interface ($v'_{\text{interface}} = -0.4$ nm/s). The black curves in (f) and (g), identify the times and locations of zero cation velocity. Below these curves, the cation velocities are negative. The time axis spans 0 to 4 h in (a), (f), and 0 to 20 min for the rest of the plots. Identical velocity color scales are used for the same velocity fields and are shown below the corresponding $v_0 = 0$ plots.

Figure 4 shows the spatial and temporal variations of species velocities starting from a uniform salt concentration, $c_{\text{avg}} = 1.00$ M ($t_+^0 \approx +0.4$), polarized at $i = 0.3$ mA/cm^2. While the solvent velocity is calculated directly from the governing equations (Eqs. [2] and [6]), the cation and anion velocities are calculated from equations [21] and [22] using the salt concentration, c, and solvent velocity, v_0, profiles. For comparison, we also show results obtained by setting $v_0 = 0$ in Eqs. [2], [21] and [22]. Starting from left, we see that the spatial and temporal variation of cation velocity, v_+, is very similar in the two cases (Figure 4(a),(f)). Considerable solvent motion is required to accommodate the salt concentration gradients in this system. The importance of this can be gauged from the spatial and temporal dependence of c_0 shown in Figure 3(b). It is therefore surprising that setting $v_0 = 0$ has such a small effect on v_+. The velocity contour lines in Figure 4(a),(f) become more-or-less vertical by $t = 2$ h, suggesting that the system is at a steady state. The main differences in v_+ are seen at early times (see Figure 4(b),(g)). The cation velocities obtained at early times after accounting for solvent motion are somewhat larger than those obtained with $v_0 = 0$. The solvent velocity is large at early times and decreases monotonically with increasing time. At a steady state, beyond $t = 2$ h, the solvent velocity is zero everywhere, as expected. We, therefore, focus on solvent motion obtained at early times in Figure 4(c). The solvent velocity is symmetrical about $x/L = 0.5$ in spite of the fact that v_+, c, and c_0 are not symmetrical functions. The solvent velocity peak occurs at $x/L = 0.5$ at all times. Since the definition of t_+^0 relates to the current carried by cation relative to solvent velocity (in a medium of uniform composition), it is instructive to examine the local cation velocity relative to the local solvent velocity $\big(v_+(x,t) - v_0(x,t)\big)$, shown in Figure 4(d) and (i). These two figures are remarkably similar, in spite of the fact that v_0 is set to zero in one case. For completeness, the spatial and temporal dependence of anion velocity, v_-, is compared in Figure 4(e) and (j). These contour plots are also symmetrical about $x/L = 0.5$. Predicted anion velocities are smaller in magnitude when solvent motion is accounted for. Including solvent motion in the model speeds up cation motion and slows down anion motion in the transient time period before the steady state is reached.

Figure 5 shows the spatial and temporal variations of species velocities starting from a uniform salt concentration, $c_{\text{avg}} = 2.58$ M ($t_+^0 \approx -0.4$), polarized at $i = 0.3$ mA/cm^2. This figure is analogous to Figure 4. Starting from left, we see that the spatial and temporal variation of cation velocity, v_+, is superficially similar in both cases (compare Figure 5(a) and (f)). The velocity contour lines in Figure 5(a),(f) become more-or-less vertical by $t = 2$ h, suggesting that the time required for equilibration is similar for $c_{\text{avg}} = 1.00$ and 2.58 M. The stark differences in v_+ are seen clearly at early times (see Figure 5(b),(g)). In this time regime, the cation velocity, relative to the electrode-electrolyte reference frame, is positive at all times when the solvent motion is accounted for. In contrast, the cation velocity based on the $v_0 = 0$ calculations, measured from the electrode reference frame, is negative for $t <$ 13 min. In other words, accounting for the divergence of the solvent velocity changes the sign of the velocity of the working ion.

The solvent velocity, shown in Figure 5(c), is more-or-less symmetric about $x/L = 0.5$ as was the case for $c_{\text{avg}} = 1.00$ M in Figure 4(c). However, with increasing time, the peak in the solvent velocity skews toward $x/L > 0.5$; at $t = 19$ min, the peak is located at $x/L = 0.55$. Figure 5(d) and (i) show that there are only minor differences in the local cation velocity relative to the local solvent velocity, $(v_+ - v_0)$. While both calculations give negative $(v_+ - v_0)$ at early times, the time window over which the negative values are seen is somewhat larger when the solvent motion is accounted for. The anion velocities obtained using the two models shown in Figure 5(e) and (j) are qualitatively similar, but the magnitude of the velocities is smaller when solvent motion is accounted for. Both sets of velocity profiles are skewed toward $x/L > 0.5$, but the skewing is less when the solvent motion is accounted for.

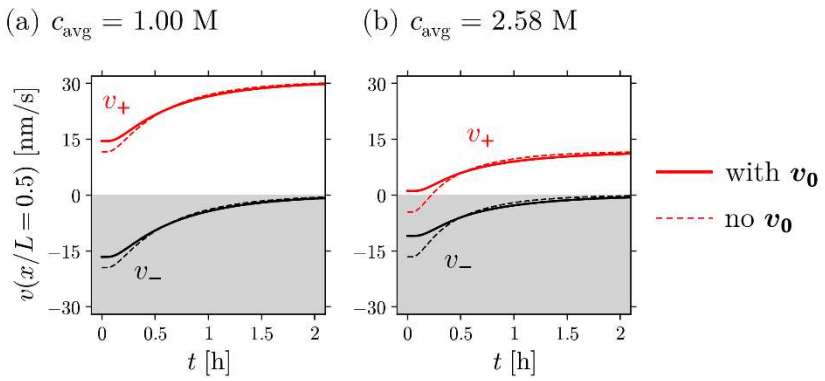

Figure 6. Ion velocities, v_+ and v_-, at the mid-point of the cell at $i = 0.3$ mA/cm^2 and the two salt concentrations discussed in Figure 4 and Figure 5, respectively. The velocities are with respect to the reference frame attached to the electrode-electrolyte interface ($v'_{\text{interface}} = -0.4$ nm/s). Dashed lines are computed velocities assuming $v_0 = 0$, while the solid lines are ion velocities when accounting for the solvent motion.

As is apparent from Eq. [20], v_0 is nonzero at all concentrations; it is nonzero even in the dilute limit ($\bar{V}(1 - t_+^0) \nrightarrow 0$ as $c \to 0$). Eqs. [21] and [22] show that the diffusion and migration terms become more dominant relative to v_0 at low values of c. Hence, the contribution of v_0 to the ion velocities becomes more significant at the higher salt concentration; compare $c_{\text{avg}} = 1.00$ M and 2.58 M in Figure 4 and Figure 5, respectively.

The key differences between the $v_0 \neq 0$ and $v_0 = 0$ calculations are shown in Figure 6 and Figure 7, where we show the time dependence of the ion velocities at the center of the cell $x/L = 0.5$. In Figure 6(a), we show the time dependence of v_+ and v_- for $c_{\text{avg}} = 1.00$ M. The two models (with solvent motion and $v_0 = 0$) give similar results. In Figure 6(b), we show the time dependence of v_+ and v_- for $c_{\text{avg}} = 2.58$ M. The significant difference is that the sign of v_+ at early times is different in the two models. Figure 6(b) shows that the cation velocity is positive at a negative t_+^0 because of solvent motion. Appendix D provides the

condition for negative v_+ at a negative t_+^0. The steady state velocities are identical in both models because $v_0 = 0$ at steady state.

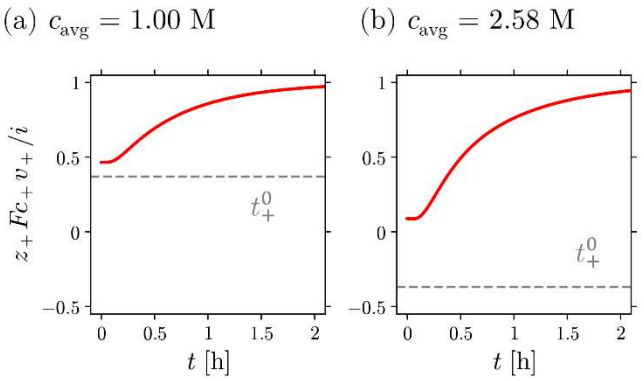

Figure 7. The ratio of the cation current, $z_+ F c_+ v_+$, to the total current at the mid-point of the cell at $i = 0.3$ mA/cm^2. The cation velocities, v_+, are with respect to a moving reference frame attached to the electrode-electrolyte interface ($v'_{\text{interface}} = -0.4$ nm/s). Comparison of the ratio to t_+^0 is instructive. The two salt concentrations, (a) $c_{\text{avg}} = 1.00$ M ($t_+^0 \approx +0.4$) and (b) $c_{\text{avg}} = 2.58$ M ($t_+^0 \approx -0.4$), used here are discussed in Figure 4 and Figure 5.

The transference number, t_+^0, is defined as the fraction of current carried by the cation relative to the solvent in the absence of concentration gradients. The current carried by the cation depends on the frame of reference, while the total current, i, does not due to charge neutrality. In Figure 7, we plot the time dependence of cation flux, $z_+ F c_+ v_+$ normalized by the total current density, i, at $x/L = 0.5$, since this ratio is often taken as the cation transference number[41–43]. At $c_{\text{avg}} = 1.00$ M, the normalized cation flux at early times, before the development of significant concentration gradients, is not very different from t_+^0, see Figure 7(a). The two quantities are not identical because of differences in the reference frames. At $c_{\text{avg}} = 2.58$ M, the normalized cation flux at early times is very different from t_+^0, see Figure 7(b). The normalized cation flux is positive, while t_+^0 is negative. Accounting for solvent motion is important when transference numbers are estimated from ion velocities[44].

It is important to note that solvent motion and reference frames are taken into account when experimental data are used to determine the transport properties, κ, D, t_+^0.[45–48] κ reflects the motion of both ions and is thus independent of solvent motion and reference frames. Solvent motion is present during the measurement of both D and t_+^0; our use of concentrated solution theory to interpret the data ensures that this motion is accounted for[19,49,50]. The properties in Our framework applies to any binary electrolyte, provided all the properties in the governing equations are known functions of concentration. This is the case for LiTFSI/PEO mixtures. The dependence of $\bar{V}$, thermodynamic factor, κ, t_+^0, and D are given in Figure 2(c)-(g). The measured values of these properties, necessary for our calculations, are also listed in **Error! Not a valid bookmark self-reference.**.

Table 1 and Figure 2(f), (g) are thus measured consistently with the framework developed in this paper.

The electric potential field, ϕ, does not have to be computed to examine concentrations and ion velocities during a galvanostatic polarization. $\Delta\phi$ was computed as a function of time using Eq. [23]. These results are unremarkable, and we do not show them for brevity.

Conclusions

Concentrated solution theory provides a framework for predicting concentration profiles and ion velocities in a binary electrolyte when a current passes through it[1]. We have used this framework to derive an expression for the divergence of the solvent velocity. This expression can be combined with the material balance equation to predict ion velocities provided two thermodynamic properties, ρ and $\left(1+\frac{d\ln f_{\pm}}{d\ln c}\right)$, and three transport properties, κ, D, and t_+^0, are known functions of salt concentration.

These governing equations are solved to examine ion transport in two LiTFSI/PEO mixtures $\left(c_{\text{avg}} = 1.00 \text{ and } 2.58 \text{ M}\right)$ in a symmetric Li-Li cell under constant current polarization. We chose these concentrations because $t_+^0 \approx +0.4$ at 1.00 M and $t_+^0 \approx -0.4$ at 2.58 M. Our main objective is to examine the velocity of the working ion (the cation) based on the electrode-electrolyte interface reference frame as a function of space and time. At $c_{\text{avg}} = 1.00$ M, the dependence of the cation velocity, v_+, on space and time follows the expected trend. In fact, the calculated values of v_+ when we neglect solvent velocity ($v_0 = 0$) are similar to those obtained after accounting for the solvent motion. At $c_{\text{avg}} = 2.58$ M, however, the obtained trends differ in the two calculations. Since $t_+^0 < 0$ at $c_{\text{avg}} = 2.58$ M, when v_0 is set to zero, the cation velocity is pointed opposite to the current flow. However, the cation velocity is along the current flow when solvent motion is accounted for, in spite of the fact that $t_+^0 \approx -0.4$. At $c_{\text{avg}} = 2.58$ M, if all other properties are kept constant, reversal of the direction of the cation velocity is obtained only when $t_+^0 < -0.5$.

These predictions are especially relevant for techniques such as electrophoretic NMR[41,51,52] and x-ray photon correlation spectroscopy[53] where ion velocities are measured directly in the laboratory reference frame. Similarly, the solvent motion is also relevant in interpreting the spatial and temporal distribution of salt concentrations as observed using magnetic resonance imaging[54,55], x-ay absorption microscopy[53,56], Raman microscopy[57], *etc.* in polarized electrolytes.

Acknowledgments

This work was supported by the Joint Center for Energy Storage Research (JCESR), an Energy Innovation Hub funded by the U.S. Department of Energy (DOE), Office of Science, Basic Energy Sciences (BES).

A.M. also appreciates discussions with Dennis Dees on the literature understanding of solvent flux in concentrated electrolytes.

The submitted manuscript has been created by UChicago Argonne, LLC, Operator of Argonne National Laboratory ("Argonne"). Argonne, a U.S. Department of Energy Office of Science laboratory, is operated under Contract No. DE-AC02-06CH11357. The U.S. Government retains for itself, and others acting on its behalf, a paid-up nonexclusive, irrevocable worldwide license in said article to reproduce, prepare derivative works, distribute copies to the public, and perform publicly and display publicly, by or on behalf of the Government. The Department of Energy will provide public access to these results of federally sponsored research in accordance with the DOE Public Access Plan. http://energy.gov/downloads/doe-public-access-plan

Nomenclature

c, salt concentration, M

c_0, solvent concentration, M

D, salt diffusion coefficient, cm^2/s, Figure 2(g)

F, Faraday's constant, 96487 C/mol

$f_\pm$, activity coefficient, *unitless*, thermodynamic factor = $\left(1 + \frac{\mathrm{d}\ln f_\pm}{\mathrm{d}\ln c}\right)$, Figure 2(d)

i, current density, mA/cm^2

L, electrolyte thickness, 500 μm

M_+, molar mass of Li^+ cations, 6.94 g/mol

M_-, molar mass of $TFSI^-$ anions, 280.15 g/mol

M_0, molar mass of PEO, 44.05 g/mol

M_{Li}, molar mass of Li, 6.94 g/mol

N, species molar flux, mol/cm^2·s

N_{grid}, finite volumes used for numerical solution, 50, Appendix B

R, Universal gas constant, 8.314 J/mol·K

T, temperature, 90°C = 363 K

t, time, s

Δt, time step used for numerical solution, 0.1 s, Appendix B

t_+^0, cation transference number relative to solvent motion, *unitless*, Figure 2(f)

$\bar{V}$, partial molar volumes, cm^3/mol, Figure 2(c)

v, velocities in the interface reference frame, nm/s

v', velocities in the stationary frame, nm/s

x, spatial coordinate, μm

Δx, space step for numerical solution, 10 μm, Appendix B

z, species charge, *unitless*

Greek Symbols

κ, ionic conductivity, S/cm, Figure 2(e)

μ, (electro-)chemical potential, J/mol

ν, stoichiometric coefficients, *unitless*, $\nu = \nu_+ + \nu_-$

ρ, electrolyte density, g/cm^3, Figure 2(a)

ρ_{Li}, density of Li, 0.534 g/cm^3

ϕ, electric potential, V

Abbreviations

NMR, Nuclear Magnetic Resonance

PEO, poly(ethylene oxide) polymer

LiTFSI, lithium bis(trifluoromethanesulfonyl)imide salt, $LiC_2F_6NO_4S_2$

Subscripts

$+$, cation

$-$, anion

0, solvent

avg, spatially average field

Appendix A. Electrolyte Thickness Change with Polarization

Since an identical amount of Li^+ is added and removed from the two reacting interfaces when the electrolyte is polarized as shown in Figure 1, the electrolyte mass is always constant. The total salt moles are also invariant. Mathematically, these facts are expressed as:

$$\rho\big(c(x,0)\big)L(0) = \int_0^{L(t)} \rho\big(c(x,t)\big)\,\mathrm{d}x\,, \qquad [24]$$

$$c(x,0)L(0) = \int_0^{L(t)} c(x,t)\,\mathrm{d}x\,, \qquad [25]$$

where (0) represents the initial uniform distribution, and t refers to corresponding fields at a later time. Note that ρ is a function of the salt concentration and varies in space and time because of any spatiotemporal changes in the c profile.

Let the electrolyte density exhibit a concentration dependence of the form $\rho = \rho_0 + \rho_1 c + \cdots$. Here $\rho_0, \rho_1, \ldots$ are coefficients and $\cdots$ represents higher order concentration dependence (the first two terms specify the linear dependence). Substituting $\rho(c)$ in Eq. [24]:

$$\rho\big(c(x,0)\big) = \frac{1}{L(0)}\int_0^{L(t)} (\rho_0 + \rho_1 c(x,t) + \cdots)\,\mathrm{d}x\,,$$

$$\therefore \rho\big(c(x,0)\big) = \frac{1}{L(0)}\left(\rho_0 L(t) + \rho_1 c(x,0)L(0) + \int_0^{L(t)} \cdots \mathrm{d}x\right)$$

where the second term on the right is simplified using Eq. [25]. If the density only varies linearly with the salt concentration, the last term vanishes:

$$\rho\big(c(x,0)\big) = \frac{1}{L(0)}\big(\rho_0 L(t) + \rho_1 c(x,0)L(0)\big)\,.$$

For $\rho = \rho_0 + \rho_1 c$, the above identity can be rearranged to show that $L(t) = L(0)$.

In general, $L(t) \neq L(0)$. The concentration dependence of the electrolyte density for LiTFSI/PEO can be obtained by regression through data as (see Nomenclature for units):

$$\rho = 1.123276 + 0.106822c + 0.007606c^2\,. \qquad [26]$$

Since the electrolyte density for LiTFSI/PEO, Eq. [26], exhibits a weak quadratic dependence, the electrolyte thickness is strictly not constant; however, its variation with time is much weaker. To characterize the time evolution of electrolyte thickness, Eq. [24] can be used as

$$\frac{L(t)}{L(0)} = \frac{\rho\big(c(x,0)\big)}{\frac{1}{L(t)}\int_0^{L(t)} \rho \, \mathrm{d}x} = \frac{\rho\big(c(x,0)\big)}{\rho_{\mathrm{avg}}}, \qquad [27]$$

where the salt concentration is used to compute the density profile at every time instance.

Figure A1 presents such calculations for the two salt concentrations, 1.00 M ($t_+^0 \approx +0.4$) and 2.58 M LiTFSI/PEO ($t_+^0 \approx -0.4$), polarized at $i = 0.3$ mA/cm^2. Here $\delta L = L(t) - L(0)$. Figure A1 shows that the electrolyte thickness change is negligible. Figure A1 also shows that

$$\frac{dL}{dt} \ll v_{\mathrm{interface}}$$

for the present calculations.

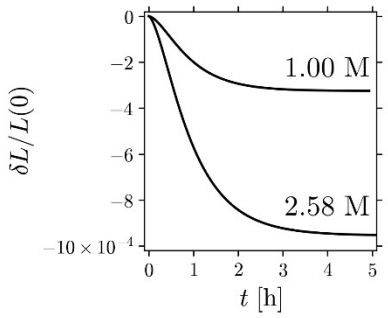

Figure A1. Change in the normalized electrolyte thickness, $\delta L/L(0)$, when the electrolyte is polarized at $i = 0.3$ mA/cm^2. The two salt concentrations, $c_{\mathrm{avg}} = 1.00$ M and $c_{\mathrm{avg}} = 2.58$ M, used here, are discussed in Figure 4 and Figure 5.

Appendix B. Details of the Numerical Solution

A computational grid is shown in Figure B1(a). The finite volume method is used to solve the governing equations. Concentrations are stored at centroids of finite volumes, while velocities are recorded at interfaces between consecutive finite volumes. The central difference scheme is used for spatial discretizations, and explicit time marching is employed for time derivatives. Accordingly, two numerical parameters, space step, Δx, and time step, Δt, are introduced. Figure B1(b)-(d) record the effect of $\Delta x = L/N_{\mathrm{grid}}$ by varying N_{grid}. Note that the variations are much smaller compared to Figure 4 and Figure 5 . Subsequently, $N_{\mathrm{grid}} = 50$ is used for all calculations. $\Delta t = 0.1$ s is kept constant across all calculations. It gives

$$\max\left(\frac{D\left(1-\frac{\mathrm{d}\ln c_0}{\mathrm{d}\ln c}\right)\Delta t}{\Delta x^2}\right) = 0.015 \ll 0.5\,, \qquad [28]$$

and satisfies the constraint for a stable solution during explicit time marching[58].

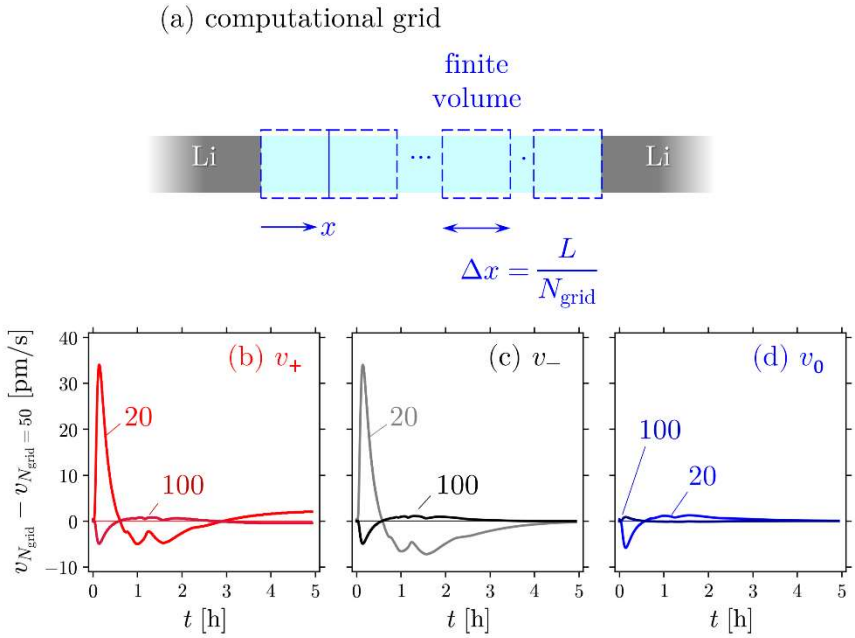

Figure B1. The effect of grid size on calculated species velocities. The velocities at the mid-point $(x/L = 0.5)$ reported in this work correspond to 50 grid points. The difference between that value and those obtained using 20 and 100 grid points is shown as a function of time. The electrolyte is 1.00 M LiTFSI/PEO and is polarized at 0.3 mA/cm² – the same as in Figure 4.

Appendix C. Determining Concentration Dependence of Thermodynamic Properties related to Density

Using Eq. [26] for $\rho = \rho(c)$, the concentration dependence of $c_0, \bar{V}, \bar{V}_0, \left(1-\frac{\mathrm{d}\ln c_0}{\mathrm{d}\ln c}\right)$ can be computed using the following expressions:

$$c_0 = \frac{1}{M_0}(\rho - Mc)\,, \qquad [29]$$

$$\bar{V} = \frac{M - \frac{\mathrm{d}\rho}{\mathrm{d}c}}{\rho - c\frac{\mathrm{d}\rho}{\mathrm{d}c}}, \qquad [30]$$

$$\bar{V}_0 = \frac{M_0}{\rho - c\dfrac{\mathrm{d}\rho}{\mathrm{d}c}}, \qquad [31]$$

$$\left(1 - \frac{\mathrm{d}\ln c_0}{\mathrm{d}\ln c}\right) = \frac{1}{c_0\bar{V}_0}. \qquad [32]$$

Appendix D. Criterion for Observing Negative Cation Velocities

The cation velocity (Eq. [21]) at $t = 0^+$, immediately after current is applied is given by

$$v_+ = \frac{1}{c}t_+^0\frac{i}{\nu_+ z_+ F} + v_0\,. \qquad [33]$$

Substituting for v_0 from Eq. [20],

$$v_+ = \frac{1}{c}t_+^0\frac{i}{\nu_+ z_+ F} + \bar{V}(1 - t_+^0)\frac{i}{\nu_+ z_+ F}. \qquad [34]$$

Based on Eq. [34], the criterion for negative v_+ is,

$$t_+^0 + c\bar{V}(1 - t_+^0) < 0\,, \qquad [35]$$

i.e.,

$$t_+^0 < \frac{-c\bar{V}}{c_0\bar{V}_0}. \qquad [36]$$

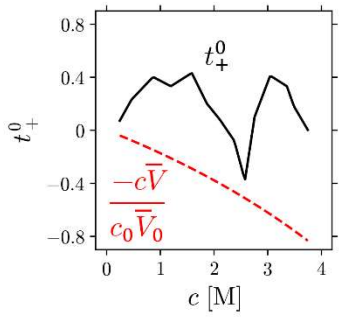

Figure D1. The solid curve shows t_+^0 as a function of c for LiTIFS/PEO. The dashed curve represents $t_+^0 = -c\bar{V}/c_0\bar{V}_0$ for LiTFSI/PEO. The cation velocity measured from the interface reference frame would have been negative if t_+^0 at a given concentration were below the dashed curve.

We show in Figure D1 that the dependence of t_+^0 on c in LiTFSI/PEO is such that inequality [36] is never satisfied.

References

(1) Newman, J.; Balsara, N. P. *Electrochemical Systems, 4e*; John Wiley & Sons, 2021.

(2) Monroe, C.; Newman, J. Dendrite Growth in Lithium/Polymer Systems: A Propagation Model for Liquid Electrolytes under Galvanostatic Conditions. *J. Electrochem. Soc.* **2003**, *150* (10), A1377–A1384. https://doi.org/10.1149/1.1606686.

(3) Wei, S.; Cheng, Z.; Nath, P.; Tikekar, M. D.; Li, G.; Archer, L. A. Stabilizing Electrochemical Interfaces in Viscoelastic Liquid Electrolytes. *Sci. Adv.* **2018**, *4* (3). https://doi.org/10.1126/sciadv.aao6243.

(4) Yang, Y.; Yin, Y.; Davies, D. M.; Zhang, M.; Mayer, M.; Zhang, Y.; Sablina, E. S.; Wang, S.; Lee, J. Z.; Borodin, O.; Rustomji, C. S.; Meng, Y. S. Liquefied Gas Electrolytes for Wide-Temperature Lithium Metal Batteries. *Energy Environ. Sci.* **2020**, *13* (7), 2209–2219. https://doi.org/10.1039/D0EE01446J.

(5) Mistry, A.; Fear, C.; Carter, R.; Love, C. T.; Mukherjee, P. P. Electrolyte Confinement Alters Lithium Electrodeposition. *ACS Energy Lett.* **2019**, *4* (1), 156–162. https://doi.org/10.1021/acsenergylett.8b02003.

(6) Mistry, A.; Srinivasan, V. On Our Limited Understanding of Electrodeposition. *MRS Adv.* **2019**, *4* (51–52), 2843–2861. https://doi.org/10.1557/adv.2019.443.

(7) Safari, M.; Kwok, C. Y.; Nazar, L. F. Transport Properties of Polysulfide Species in Lithium-Sulfur Battery Electrolytes: Coupling of Experiment and Theory. *ACS Cent. Sci.* **2016**, *2* (8), 560–568. https://doi.org/10.1021/acscentsci.6b00169.

(8) Mistry, A. N.; Mukherjee, P. P. Electrolyte Transport Evolution Dynamics in Lithium-Sulfur Batteries. *J. Phys. Chem. C* **2018**, *122* (32), 18329–18335. https://doi.org/10.1021/acs.jpcc.8b05442.

(9) Forner-Cuenca, A.; Penn, E. E.; Oliveira, A. M.; Brushett, F. R. Exploring the Role of Electrode Microstructure on the Performance of Non-Aqueous Redox Flow Batteries. *J. Electrochem. Soc.* **2019**, *166* (10), A2230–A2241. https://doi.org/10.1149/2.0611910jes.

(10) Mistry, A.; Trask, S.; Dunlop, A.; Jeka, G.; Polzin, B.; Mukherjee, P. P.; Srinivasan, V. Quantifying Negative Effects of Carbon-Binder Networks from Electrochemical Performance of Porous Li-Ion Electrodes. *J. Electrochem. Soc.* **2021**, *168* (7), 70536. https://doi.org/10.1149/1945-7111/ac1033.

(11) Fredericks, W. L.; Sripad, S.; Bower, G. C.; Viswanathan, V. Performance Metrics Required of Next-Generation Batteries to Electrify Vertical Takeoff and Landing (VTOL) Aircraft. *ACS Energy Lett.* **2018**, *3* (12), 2989–2994. https://doi.org/10.1021/acsenergylett.8b02195.

(12) Ferraro, M. E.; Trembacki, B. L.; Brunini, V. E.; Noble, D. R.; Roberts, S. A. Electrode Mesoscale as a Collection of Particles: Coupled Electrochemical and Mechanical Analysis of NMC Cathodes. *J. Electrochem. Soc.* **2020**, *167* (1), 013543. https://doi.org/10.1149/1945-7111/ab632b.

(13) Mistry, A. N.; Usseglio-Viretta, F. L. E.; Colclasure, A. M.; Smith, K.; Mukherjee, P. P. Fingerprinting Redox Heterogeneity in Electrodes during Extreme Fast Charging. *J. Electrochem. Soc.* **2020**, *167* (9), 090542. https://doi.org/10.1149/1945-7111/ab8fd7.

(14) Colclasure, A. M.; Tanim, T. R.; Jansen, A. N.; Trask, S. E.; Dunlop, A. R.; Polzin, B. J.; Bloom, I.; Robertson, D.; Flores, L. R.; Evans, M.; Dufek, E. J.; Smith, K. Electrode Scale and Electrolyte Transport Effects on Extreme Fast Charging of Lithium-Ion Cells. *Electrochim. Acta* **2020**, *337*, 135854. https://doi.org/10.1016/j.electacta.2020.135854.

(15) Forouzan, M. M.; Mazzeo, B. A.; Wheeler, D. R. Modeling the Effects of Electrode Microstructural Heterogeneities on Li-Ion Battery Performance and Lifetime. *J. Electrochem. Soc.* **2018**, *165* (10), A2127–A2144. https://doi.org/10.1149/2.1281809jes.

(16) Colclasure, A. M.; Dunlop, A. R.; Trask, S. E.; Polzin, B. J.; Jansen, A. N.; Smith, K. Requirements for Enabling Extreme Fast Charging of High Energy Density Li-Ion Cells While Avoiding Lithium Plating. *J. Electrochem. Soc.* **2019**, *166* (8), A1412–A1424. https://doi.org/10.1149/2.0451908jes.

(17) Smart, M. C.; Ratnakumar, B. V.; Surampudi, S. Electrolytes for Low-Temperature Lithium Batteries Based on Ternary Mixtures of Aliphatic Carbonates. *J. Electrochem. Soc.* **1999**, *146* (2), 486–492. https://doi.org/10.1149/1.1391633.

(18) Kim, H.-K.; Balsara, N. P.; Srinivasan, V. Continuum Description of the Role of Negative Transference Numbers on Ion Motion in Polymer Electrolytes. *J. Electrochem. Soc.* **2020**, *167* (11), 110559. https://doi.org/10.1149/1945-7111/aba790.

(19) Pesko, D. M.; Timachova, K.; Bhattacharya, R.; Smith, M. C.; Villaluenga, I.; Newman, J.; Balsara, N. P. Negative Transference Numbers in Poly(Ethylene Oxide)-Based Electrolytes. *J. Electrochem. Soc.* **2017**, *164* (11), E3569–E3575. https://doi.org/10.1149/2.0581711jes.

(20) Pesko, D. M.; Feng, Z.; Sawhney, S.; Newman, J.; Srinivasan, V.; Balsara, N. P. Comparing Cycling Characteristics of Symmetric Lithium-Polymer-Lithium Cells with Theoretical Predictions. *J. Electrochem. Soc.* **2018**, *165* (13), A3186–A3194. https://doi.org/10.1149/2.0921813jes.

(21) Newman, J.; Bennion, D.; Tobias, C. W. Mass Transfer in Concentrated Binary Electrolytes. *Berichte der Bunsengesellschaft für Phys. Chemie* **1965**, *69* (7), 608–612. https://doi.org/10.1002/bbpc.19650690712.

(22) Guggenheim, E. A.; Woolley, H. W. *Thermodynamics: An Advanced Treatment for Chemists and Physicists*, 7th ed.; North-Halland Physics, 1985. https://doi.org/10.1063/1.3060168.

(23) Christensen, J.; Newman, J. A Mathematical Model for the Lithium-Ion Negative Electrode Solid Electrolyte Interphase. *J. Electrochem. Soc.* **2004**, *151* (11), A1977. https://doi.org/10.1149/1.1804812.

(24) Uppaluri, M.; Subramaniam, A.; Mishra, L.; Viswanathan, V.; Subramanian, V. R. Can a Transport Model Predict Inverse Signatures in Lithium Metal Batteries Without Modifying Kinetics? *J. Electrochem. Soc.* **2021**, *167* (16), 160547. https://doi.org/10.1149/1945-7111/abd2ae.

(25) Mishra, L.; Subramaniam, A.; Jang, T.; Shah, K.; Uppaluri, M.; Roberts, S. A.; Subramanian, V. R. Perspective—Mass Conservation in Models for Electrodeposition/Stripping in Lithium Metal Batteries. *J. Electrochem. Soc.* **2021**, *168* (9), 92502. https://doi.org/10.1149/1945-7111/ac2091.

(26) Newman, J.; Chapman, T. W. Restricted Diffusion in Binary Solutions. *AIChE J.* **1973**, *19* (2), 343–348. https://doi.org/https://doi.org/10.1002/aic.690190220.

(27) Liu, J.; Monroe, C. W. Solute-Volume Effects in Electrolyte Transport. *Electrochim. Acta* **2014**, *135*, 447–460. https://doi.org/10.1016/j.electacta.2014.05.009.

(28) Wang, A. A.; Gunnarsdóttir, A. B.; Fawdon, J.; Pasta, M.; Grey, C. P.; Monroe, C. W. Potentiometric MRI of a Superconcentrated Lithium Electrolyte: Testing the Irreversible Thermodynamics Approach. *ACS Energy Lett.* **2021**, *6* (9), 3086–3095. https://doi.org/10.1021/acsenergylett.1c01213.

(29) Gallagher, K. G.; Dees, D. W.; Jansen, A. N.; Abraham, D. P.; Kang, S.-H. A Volume Averaged Approach to the Numerical Modeling of Phase-Transition Intercalation Electrodes Presented for Li x C 6 . *J. Electrochem. Soc.* **2012**, *159* (12), A2029–A2037. https://doi.org/10.1149/2.015301jes.

(30) Dees, D. W.; Kawauchi, S.; Abraham, D. P.; Prakash, J. Analysis of the Galvanostatic Intermittent Titration Technique (GITT) as Applied to a Lithium-Ion Porous Electrode. *J. Power Sources* **2009**, *189* (1), 263–268. https://doi.org/https://doi.org/10.1016/j.jpowsour.2008.09.045.

(31) Hauser, A. K.; Newman, J. The Effect of Schmidt Number on the Faradaic Impedance of the Dissolution of a Copper Rotating Disk. *J. Electrochem. Soc.* **1989**, *136* (10), 2896–2902. https://doi.org/10.1149/1.2096316.

(32) Gu, W. B.; Wang, C. Y.; Liaw, B. Y. Numerical Modeling of Coupled Electrochemical and Transport Processes in Lead-Acid Batteries. *J. Electrochem. Soc.* **1997**, *144* (6), 2053–2061. https://doi.org/10.1149/1.1837741.

(33) Crothers, A. R.; Darling, R. M.; Kushner, D. I.; Perry, M. L.; Weber, A. Z. Theory of Multicomponent Phenomena in Cation-Exchange Membranes: Part III. Transport in Vanadium Redox-Flow-Battery Separators. *J. Electrochem. Soc.* **2020**, *167* (1), 13549. https://doi.org/10.1149/1945-7111/ab6725.

(34) H. Hashemi, S. M.; Karnakov, P.; Hadikhani, P.; Chinello, E.; Litvinov, S.; Moser, C.; Koumoutsakos, P.; Psaltis, D. A Versatile and Membrane-Less Electrochemical Reactor for the Electrolysis of Water and Brine. *Energy Environ. Sci.* **2019**, *12* (5), 1592–1604. https://doi.org/10.1039/C9EE00219G.

(35) Gu, W. B.; Wang, C. Y.; Weidner, J. W.; Jungst, R. G.; Nagasubramanian, G. Computational Fluid Dynamics Modeling of a Lithium/Thionyl Chloride Battery with Electrolyte Flow. *J. Electrochem. Soc.* **2000**, *147* (2), 427. https://doi.org/10.1149/1.1393213.

(36) Kwak, R.; Pham, V. S.; Han, J. Sheltering the Perturbed Vortical Layer of Electroconvection under Shear Flow. *J. Fluid Mech.* **2017**, *813*, 799–823. https://doi.org/DOI: 10.1017/jfm.2016.870.

(37) Weber, A. Z.; Newman, J. Transport in Polymer-Electrolyte Membranes: II. Mathematical Model. *J. Electrochem. Soc.* **2004**, *151* (2), A311–A325. https://doi.org/10.1149/1.1639157.

(38) Fuller, T. F.; Newman, J. Experimental Determination of the Transport Number of Water in Nafion 117 Membrane. *J. Electrochem. Soc.* **1992**, *139* (5), 1332–1337. https://doi.org/10.1149/1.2069407.

(39) Monroe, C. W. Does Oxygen Transport Affect the Cell Voltages of Metal/Air Batteries? *J. Electrochem. Soc.* **2017**, *164* (11), E3547–E3551. https://doi.org/10.1149/2.0521711jes.

(40) Mistry, A. N.; Cano-Banda, F.; Law, D.; Hernandez-Guerrero, A.; Mukherjee, P. P. Non-Equilibrium Thermodynamics in Electrochemical Complexation of Li-Oxygen Porous Electrodes. *J. Mater. Chem. A* **2019**, *7* (15), 8882–8888. https://doi.org/10.1039/c9ta01339c.

(41) Walls, H. J.; Zawodzinski, T. A. Anion and Cation Transference Numbers Determined by Electrophoretic NMR of Polymer Electrolytes Sum to Unity. *Electrochem. Solid-State Lett.* **2000**, *3* (7), 321–324. https://doi.org/10.1149/1.1391136.

(42) Dai, H.; Zawodzinski, T. A. Determination of Lithium Ion Transference Numbers by Electrophoretic Nuclear Magnetic Resonance. *J. Electrochem. Soc.* **1996**, *143* (6), L107–L109. https://doi.org/10.1149/1.1836891.

(43) Dai, H.; Zawodzinski, T. A. The Dependence of Lithium Transference Numbers on Temperature, Salt

Concentration and Anion Type in Poly (Vinylidene Fluoride)–Hexafluoropropylene Copolymer-Based Gel Electrolytes1Presented at the Electrochemical Society Symposium: Processes in Polymers A. *J. Electroanal. Chem.* **1998**, *459* (1), 111–119. https://doi.org/https://doi.org/10.1016/S0022-0728(98)00373-8.

(44) Timachova, K.; Newman, J.; Balsara, N. P. Theoretical Interpretation of Ion Velocities in Concentrated Electrolytes Measured by Electrophoretic NMR. *J. Electrochem. Soc.* **2019**, *166* (2), A264–A267. https://doi.org/10.1149/2.0591902jes.

(45) Lundgren, H.; Behm, M.; Lindbergh, G. Electrochemical Characterization and Temperature Dependency of Mass-Transport Properties of LiPF 6 in EC:DEC . *J. Electrochem. Soc.* **2015**, *162* (3), A413–A420. https://doi.org/10.1149/2.0641503jes.

(46) Hou, T.; Monroe, C. W. Composition-Dependent Thermodynamic and Mass-Transport Characterization of Lithium Hexafluorophosphate in Propylene Carbonate. *Electrochim. Acta* **2020**, *332*, 135085. https://doi.org/10.1016/j.electacta.2019.135085.

(47) Landesfeind, J.; Gasteiger, H. A. Temperature and Concentration Dependence of the Ionic Transport Properties of Lithium-Ion Battery Electrolytes. *J. Electrochem. Soc.* **2019**, *166* (14), A3079–A3097. https://doi.org/10.1149/2.0571912jes.

(48) Valøen, L. O.; Reimers, J. N. Transport Properties of LiPF[Sub 6]-Based Li-Ion Battery Electrolytes. *J. Electrochem. Soc.* **2005**, *152* (5), A882–A891. https://doi.org/10.1149/1.1872737.

(49) Ma, Y.; Doyle, M.; Fuller, T. F.; Doeff, M. M.; De Jonghe, L. C.; Newman, J. The Measurement of a Complete Set of Transport Properties for a Concentrated Solid Polymer Electrolyte Solution. *J. Electrochem. Soc.* **1995**, *142* (6), 1859–1868. https://doi.org/10.1149/1.2044206.

(50) Villaluenga, I.; Pesko, D. M.; Timachova, K.; Feng, Z.; Newman, J.; Srinivasan, V.; Balsara, N. P. Negative Stefan-Maxwell Diffusion Coefficients and Complete Electrochemical Transport Characterization of Homopolymer and Block Copolymer Electrolytes. *J. Electrochem. Soc.* **2018**, *165* (11), A2766–A2773. https://doi.org/10.1149/2.0641811jes.

(51) Zhang, Z.; Madsen, L. A. Observation of Separate Cation and Anion Electrophoretic Mobilities in Pure Ionic Liquids. *J. Chem. Phys.* **2014**, *140* (8), 84204. https://doi.org/10.1063/1.4865834.

(52) Rosenwinkel, M. P.; Schönhoff, M. Lithium Transference Numbers in PEO/LiTFSA Electrolytes Determined by Electrophoretic NMR. *J. Electrochem. Soc.* **2019**, *166* (10), A1977–A1983. https://doi.org/10.1149/2.0831910jes.

(53) Steinrück, H. G.; Takacs, C. J.; Kim, H. K.; MacKanic, D. G.; Holladay, B.; Cao, C.; Narayanan, S.; Dufresne, E. M.; Chushkin, Y.; Ruta, B.; Zontone, F.; Will, J.; Borodin, O.; Sinha, S. K.; Srinivasan, V.; Toney, M. F. Concentration and Velocity Profiles in a Polymeric Lithium-Ion Battery Electrolyte. *Energy Environ. Sci.* **2020**, *13* (11), 4312–4321. https://doi.org/10.1039/d0ee02193h.

(54) Klett, M.; Giesecke, M.; Nyman, A.; Hallberg, F.; Lindström, R. W.; Lindbergh, G.; Furó, I. Quantifying Mass Transport during Polarization in a Li Ion Battery Electrolyte by in Situ 7Li NMR Imaging. *J. Am. Chem. Soc.* **2012**, *134* (36), 14654–14657. https://doi.org/10.1021/ja305461j.

(55) Bazak, J. D.; Allen, J. P.; Krachkovskiy, S. A.; Goward, G. R. Mapping of Lithium-Ion Battery Electrolyte Transport Properties and Limiting Currents with In Situ MRI. *J. Electrochem. Soc.* **2020**, *167* (14), 140518. https://doi.org/10.1149/1945-7111/abc0c9.

(56) Takamatsu, D.; Yoneyama, A.; Asari, Y.; Hirano, T. Quantitative Visualization of Salt Concentration Distributions in Lithium-Ion Battery Electrolytes during Battery Operation Using X-Ray Phase Imaging. *J. Am. Chem. Soc.* **2018**, *140* (5), 1608–1611. https://doi.org/10.1021/jacs.7b13357.

(57) Fawdon, J.; Ihli, J.; Mantia, F. La; Pasta, M. Characterising Lithium-Ion Electrolytes via Operando Raman Microspectroscopy. *Nature Communications*. December 11, 2021. https://doi.org/10.1038/s41467-021-24297-0.

(58) Kreyszig, E. *Advanced Engineering Mathematics, Tenth Edition*; 2005. https://doi.org/10.2307/3612523.